RICE UNIVERSITY

Bleach Imaged Plasmon Propagation (BIIPP) in Single Gold Nanowires

by

David Enrique Solis Jr.

A THESIS SUBMITTED IN PARTIAL FULFILLMENT OF THE REQUIREMENTS FOR THE DEGREE

Master of Science

Approved, Thesis Committee:

Stephan Link,
Assistant Professor of Chemistry,
Assistant Professor of Electrical and Computer Engineering

Naomi Halas,
Stanley C. Moore Professor of Electrical and Computer Engineering,
Professor of Biomedical Engineering,
Chemistry, Physics & Astronomy,
Director, Laboratory for Nanophotonics

Peter Nordlander,
Professor of Physics and Astronomy,
Professor of Electrical and Computer Engineering

Houston, Texas
November 2010

ABSTRACT

Bleach Imaged Plasmon Propagation (BlIPP) in Single Gold Nanowires

by

David Solis

Here, we present a novel approach to visualize propagating surface plasmon polaritons through plasmon-exciton interactions between single gold nanowires and a thin film of a fluorescent polymer. A plasmon polariton was launched by exciting one end of a single gold nanowire with a 532 nm laser. The local near-field of the propagating plasmon modes caused bleaching of the polymer emission. The degree of photobleaching along the nanowire could be correlated with the propagation distance of the surface plasmon polaritons. Using this method of bleach-imaged plasmon propagation (BlIPP), we determined a plasmon propagation distance of 1.8 ± 0.4 μm at 532 nm for chemically grown gold nanowires. Our results are supported by finite difference time domain electromagnetic simulations.

ACKNOWLEDGEMENT

I would firstly like to thank my advisor and mentor Stephan Link for his guidance and motivation through the development of this project. With his help I have been able to develop a research project, from developing an instrument, to running an experiment and finally to publishing a paper, Stephan has truly been an inspiration to me. I would also like to give special thanks to Wei-Shun Chang for his invaluable advice, and Britain Willingham for help with the data analysis.

Special thanks to our collaborators Peter Nordlander and Kui Bao for insights into the BlIPP measurement through computational simulations. Also thanks to our collaborators in Eugene Zubarev's lab, Bishnu Khanal and Leonid Vigderman who have helped so much with the synthesis of the gold nanowire samples.

I would also like to recognize the funding which has made this research possible especially the National Science Foundation for their support through a NSF Graduate Research Fellowship. I also thank the reviewer of our recently published paper for invaluable feedback, Dr. Matthew Pelton, Dr. Christy Landes, and the Landes group for useful discussions.

Thanks to all my labmates, for the conversations and insights which have given me new perspectives essential for developing this project as well as keeping me sane. Special thanks to Bruce Johnson, who has been a great mentor and teacher in both my academic and personal life.

Finally, and most importantly, I thank my parents David and Gloria Solis, my brothers Jason and Kevin and my entire family. I am who I am because of you; words can never express how much you mean to me. This work is dedicated to you.

TABLE OF CONTENTS

Introduction to Surface Plasmon Propagation for Metallic Nanowires 1

Materials and Sample Preparation 4

Experimental Setup 6

Description of the BlIPP Method 10

Data Analysis Routine 13

Results from BlIPP Experiments 15

Finite difference time domain (FDTD) simulations 20

Conclusion 23

References 24

LIST OF FIGURES

Fig. 1.....4

Fig. 2.....7

Fig. 3.....8

Fig. 4.....9

Fig. 5.....10

Fig. 6.....16

Fig. 7.....18

Fig. 8.....20

Fig. 9.....21

Introduction to Surface Plasmon Propagation for Metallic Nanowires

One-dimensional metallic nanostructures such as nanowires (NWs), stripes, or nanoparticle chains are widely studied as potential optical waveguides.[1-9] By coupling electromagnetic waves to collective electron oscillations in the metal known as surface plasmon polaritons (SPPs),[10, 11] light can be guided over distances exceeding tens of micrometers and then emitted at the opposite end of the plasmonic waveguide.[12] Critically important in the design of metallic waveguide structures is the minimization of radiative and nonradiative losses that cause reduced SPP propagation distances. The high crystallinity and smooth surfaces of chemically prepared silver NWs have been shown to drastically improve SPP propagation distances compared to lithographically fabricated structures.[1, 3-5] For this reason, NWs are promising as interconnects in integrated optical and electronic circuits.

Chemically grown gold NWs have in principle the same advantages as silver NWs, but gold is intrinsically more lossy, especially at optical frequencies.[13] This makes it more difficult to accurately determine SPP propagation distances in gold NWs, especially if the NWs are longer than the SPP decay length. In contrast, for NWs shorter than the SPP propagation distance, excitation at one of the NW ends allows for photons to couple with SPP modes, which are then converted back into light at the opposite NW end as observed by far-field distal end emission.[3-5] Because the SPPs are also partially reflected at the NW ends creating Fabry–Perot type cavity resonances,[1, 14-16] the emitted light intensity by itself is however not a sufficient parameter for determining the SPP propagation distance. An alternate approach is to use multiple or variable input couplers positioned at different locations along the NW (e.g., sharp NW kinks, closely spaced

nanoparticle antennas, or other waveguides)[3, 5, 17] but this requires precise control over the launch sites, which can often be difficult.

A different approach, which does not rely on the conversion of SPPs back into photons and hence is applicable to NWs much longer than the propagation distance, is to directly measure the plasmon-induced near-field. This has been accomplished using, for example, near-field scanning optical microscopy or photoemission electron microscopy.[1, 16, 18, 19] Although these are excellent techniques for mapping the SPP near-field intensity and propagation distance, lower resolution far-field detection can often be less expensive, easier to implement, and more straightforward to interpret. Taking advantage of energy transfer between the SPP field and fluorescent molecules, it has been shown that the optical near-field of SPPs can be visualized using far-field fluorescence microscopy.[20, 21] However, for short SPP propagation distances the fluorescence intensity due to direct laser excitation masks the much weaker signal originating from SPP excited fluorescence. In addition, a drawback of this method can be the irreversible photobleaching of the fluorescent probe.[20] Hence, it remains an important challenge to accurately measure the SPP decay in metallic NWs to address the needs in the fast growing field of plasmonic waveguiding.

Here, we introduce a far-field method that exploits the photobleaching of a thin film of fluorescent polymer coated on top of gold NWs.[22] We demonstrate that the SPP near-field can be imaged through the bleaching of the polymer emission along the NW, thereby obtaining the SPP propagation distance. Because bleach-imaged plasmon propagation (BlIPP) does not rely on light emission at the distal NW end or input couplers along the NW, it can be applied to any plasmonic NW but is particularly suited

to measure highly damped SPPs. In particular, we applied BlIPP to determine the SPP propagation distance in chemically grown gold NWs at 532 nm, where interband absorptions strongly damp the SPPs. In conjunction with simulations, we identified several higher order SPP modes with surprisingly long propagation distances.

Materials and Sample Preparation

First, cetyltrimethylammonium bromide (CTAB) coated 30 nm wide nanowires (NWs) were synthesized by tip selective growth of purified pentahedrally twinned gold nanorods[23]. The NWs used in this study were then grown by fast side wise deposition of gold on the pre-synthesized NWs. The lengths and widths were determined by scanning electron microscopy (SEM). The gold NWs were measured to have average dimensions of 6.1 ± 1.2 μm x 400 ± 80 nm from SEM images taken at a magnification of 2,000 (Fig. 1A) and 11,000 (Fig. 1B) on a JEOL 6500F SEM operating at a voltage of 15 kV.

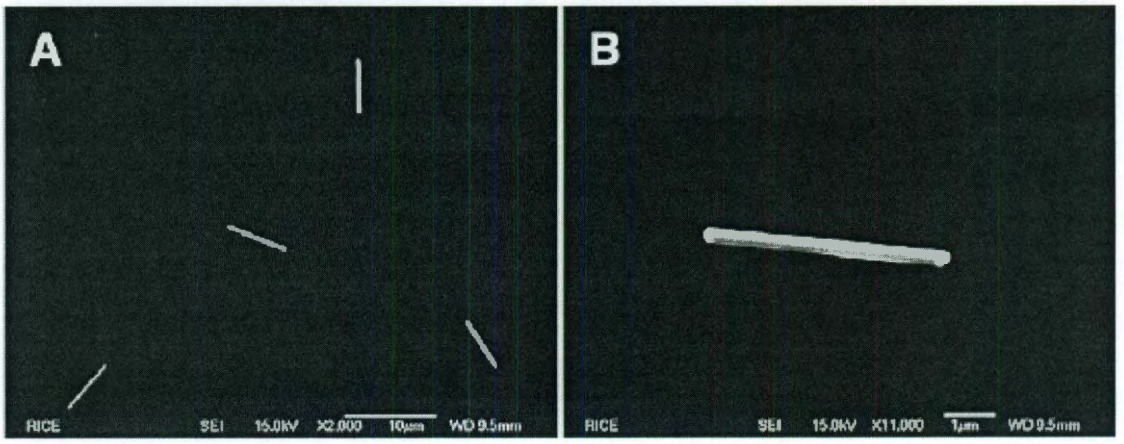

Fig. 1 (A) shows an SEM image of gold NWs taken at a magnification of 2,000. **(B)** shows an SEM of a single gold NW taken at a magnification of 11,000.

A drop of the gold NW solution was spin cast (Headway Research Inc.) at 2000 rpm for 40 seconds onto a glass coverslip (Fisher Scientific). The coverslips were first sonicated (Branson 2510) for 15 minutes in Acetone (Fisher Scientific) and then oxygen plasma cleaned (Harrick Plasma). The sample was then dipped in warm deionized water and dried with a low nitrogen flow in order to remove excess CTAB. Afterwards a 8.5*10-3 g/mL solution of poly[2-methoxy-5-(2-ethylhexyloxy)-1,4-phenylenevinylene] (MEH-PPV, M_n = 40,000-70,000, Sigma Aldrich) in toluene (Fisher Scientific) was spin

cast onto the gold NWs at 3000 rpm for 40 seconds which created a continuous 60 nm thick MEH-PPV film covering the gold NWs as well as the glass surface. The film thickness of the fluorescent polymer was measured by scratching the polymer film and imaging the scratch using atomic force microscopy (Digital Instrument Nanoscope IIIA).

Experimental Setup

Fluorescence images were acquired using a 532 nm laser excitation source (Coherent Verdi V6), an XY translation piezo stage (Physik Instrumente P-517.2CL), an inverted microscope (Zeiss Observer), a 100x magnification 0.75 NA objective (Zeiss Epiplan), and an avalanche photodiode detector (Perkin Elmer, SPCM-AQRH-15-FC). The laser beam was focused to a diffraction limited spot size (FWHM = 300 nm) at the sample. Circular and linear polarizations were controlled by a quarter and half waveplate (Thorlabs), respectively. To make sure that only fluorescence was detected, a 532 nm notch filter was placed into the detection path and an appropriate dichroic was used in the microscope. Photons collected by the detector were digitized as TTL signals and counted by a counting board (National Instruments DAQ PCI-6602). The photon counting board and scanning stage were controlled by a LabVIEW program. Typically, sample scanned fluorescence images were taken of 10 x 10 μm areas with an integration time of 5 ms/pixel and a resolution of 256 x 256 pixels. Fluorescence spectra in the wavelength range of 400 – 800 nm were acquired by redirecting the fluorescence to a monochromator (Horiba Jobin Yvon TRIAX 190) coupled to a liquid nitrogen cooled CCD camera (Horiba Jobin Yvon Symphony). Note that the MEH-PPV film covered both the NW and the surrounding area and was facing the excitation light. The laser focus was optimized carefully for each measurement.

Fluorescence spectra of a MEH-PPV coated gold NW sample recorded with a 10 seconds exposure time and an excitation power of 34 pW are shown in Fig. 2A. The fluorescence spectrum taken from an area on top of a gold NW is indistinguishable from

the MEH-PPV fluorescence collected next to the NW. This shows that only the intensity was enhanced while the spectrum of the conductive polymer did not change.

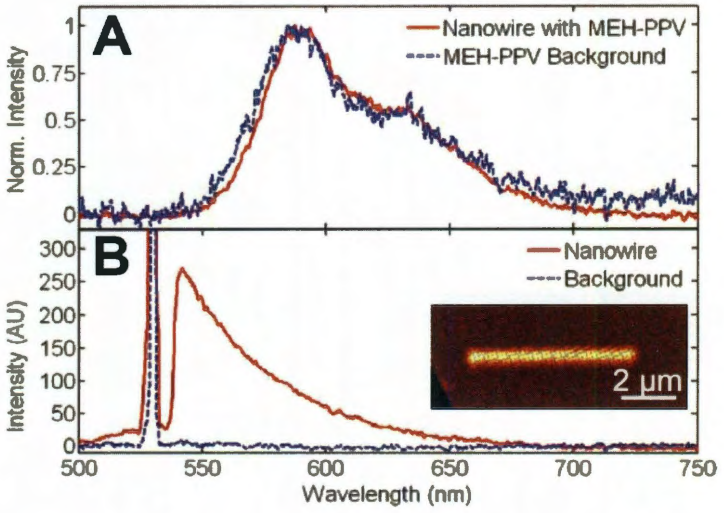

Fig. 2 (A) shows spectra taken from a MEH-PPV coated gold NW sample on (red solid line) and next to (blue dashed line) a single NW. The excitation power was 34 pW. **(B)** shows spectra taken from a non-coated NW sample on (red solid line) and next to (blue dashed line) a single NW. The inset shows a fluorescence image of a non-coated gold NW. The peak at 532 nm corresponds to the laser excitation wavelength which could not be entirely blocked at a higher laser power of 109 μW.

To ensure that intrinsic luminescence from the NW did not contribute to the observed intensity, we measured the fluorescence image of the gold NW before coating it with the MEH-PPV film. At the same excitation power as used for the NW – MEH-PPV sample we did not observe any luminescence from the gold NW. Only after increasing the laser power by more than a million was the intrinsic luminescence from the NW detectable. Fig. 2B shows the luminescence spectrum of a gold NW using an excitation power of 109 mW. A fluorescence image of a non-coated gold NW is shown in the inset. The background spectrum in Fig. 2B was collected with the laser positioned next to the NW. All spectra were corrected by subtracting detector dark counts.

We also performed a power dependence measurement for the MEH-PPV fluorescence collected from an area above a gold NW. The normalized spectra are shown

in Fig. 3 and the inset is a plot of the fluorescence intensity at the maximum wavelength (610 nm) vs. laser power. The spectra slightly broaden with increasing excitation power as also observed for spectra of MEH-PPV without gold NWs present. More importantly, no spectral narrowing indicative of stimulated emission was observed as otherwise expected for gain due to plasmon-exciton interactions. The intensity furthermore follows initially a linear power dependence and then saturates at higher excitation powers, probably due to photobleaching (see inset).

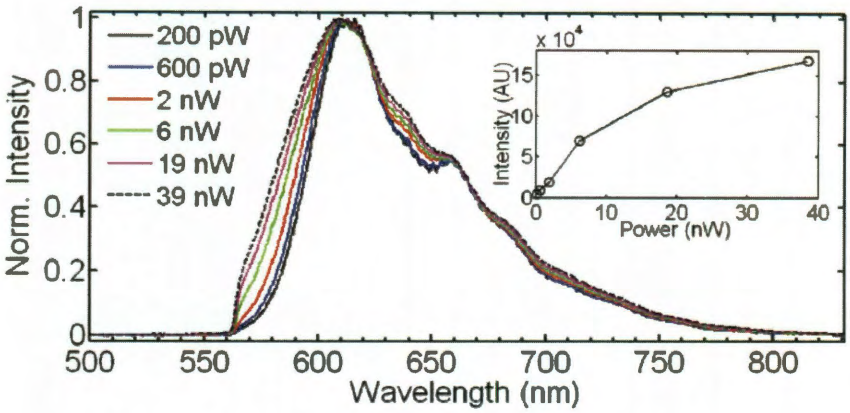

Fig. 3 Fluorescence spectra taken from a MEH-PPV coated gold NW as a function of excitation power. The inset shows a plot of the fluorescence intensity at the maximum wavelength vs. laser power

The fluorescence enhancement of the MEH-PPV film was found to be independent on the laser polarization. Fig. 4 illustrates that fluorescence images of a MEH-PPV coated gold NW showed no difference in the measured intensity when light polarized parallel (Fig. 4A) or perpendicular (Fig. 4B) to the long NW axis was used. The excitation power was carefully adjusted to the same value of 30 pW for both laser polarizations.

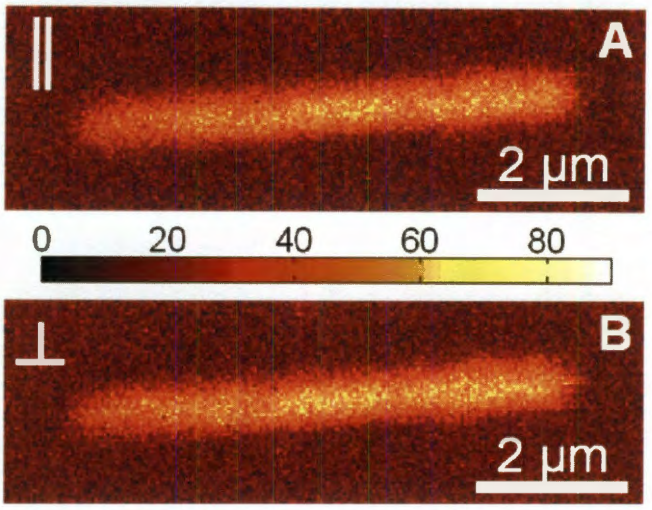

Fig. 4 (A) shows a sample scanned fluorescence image of a MEH-PPV coated NW. The excitation source was polarized parallel to the long axis of the NW. **(B)** shows a sample scanned fluorescence image of the same NW as in Fig. 4A except that in this image the excitation source was polarized perpendicular to the long axis of the NW. The laser power for both images was 30 pW.

Description of the BlIPP Method

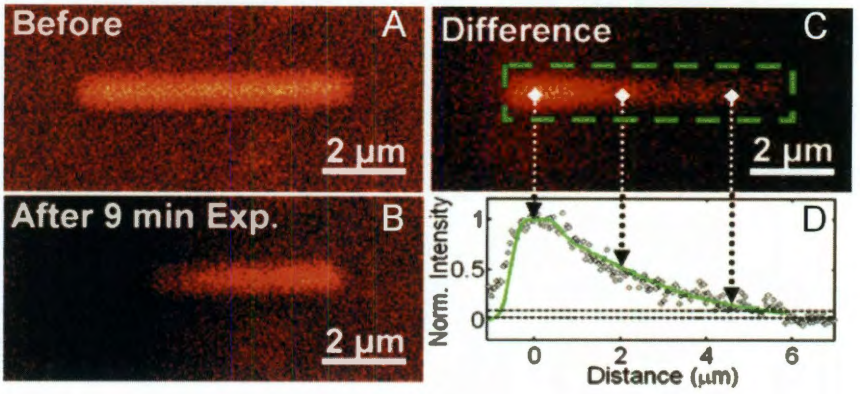

Fig. 5 (A) Shows a fluorescence image taken over an area with Au NW present as shown by the area with enhanced fluorescence signal. **(B)** Shows the fluorescence image of the same area taken after a 9 min high power laser exposure. **(C)** Shows the difference image created by subtracting (B) from (C). The green highlighted area is then made into a width averaged line section as shown in **(D). (D)** Also shows a green line which is a fit of the data using the derived bleach intensity function, Eq. 5.

For the BlIPP experiments, a fluorescence image was first taken of a single MEH-PPV coated gold NW using a low excitation power of a few picowatts, shown in Fig. 5A. The excitation power was adjusted with neutral density filters so that the fluorescence collected from on top of a NW was around 50 counts per 10 ms integration time. The exact power therefore varied slightly from NW to NW, probably due to a small variation in the thickness of the MEH-PPV film. The piezo scanning stage was then positioned such that the laser was focused onto one end of the gold NW and the laser power was raised by a factor of 10,000 (OD filter of 4) for a certain exposure time.

During laser exposure at the gold NW tip, photons met the momentum matching criterion due to the sharp break in symmetry at the NW tip and successfully launched surface plasmon polaritons (SPPs). Because of the MEH-PPV coating, the propagating SPP waves along the gold NW interacted with excitons of the MEH-PPV causing the MEH-PPV near the gold NW to fluoresce. At high excitation powers and long exposure

times the MEH-PPV photobleached due to both direct laser excitation at the focal point near the NW tip and along the gold NW due to plasmon-exciton coupling.

To probe the MEH-PPV photobleaching, the laser power was lowered again to the previous level and a second fluorescence image was taken of the same area, Fig. 5B. Therefore a destructive technique, namely photobleaching, was used to image plasmon propagation along the gold NW. Note that the laser power and exposure time per pixel were so low for the acquisition of the fluorescence images that photobleaching can safely be neglected. It also needs to be mentioned that during the continuous laser exposure we ensured that the laser remained in focus and sample drift was minimal. For each fluorescence image, the microscope focus was furthermore carefully optimized.

To create images of photobleach intensity the second image taken after the laser exposure was subtracted from the initial image using a program written in MATLAB (version R2007b). This created a difference image shown in Fig. 5C, which visualized the effect of SPP assisted photobleaching of the MEH-PPV thin film coating. The difference image was analyzed to determine the SPP propagation distance as outlined in the next section.

However, before subtracting the two fluorescence images obtained before and after photobleaching, a background correction factor was determined to correct for small fluctuations in background intensity either due to a slightly different focus or small change in laser power. The background correction factor was calculated by choosing a small background area of 40 x 40 pixels from the same areas in both fluorescence images. All pixels in these areas were first averaged and then their ratio determined, thus yielding the correction factor.

Next, in order to create a width averaged photobleach intensity line section along the long NW axis from the difference image, the width of the NW in the image was first determined by taking an intensity line section perpendicular to the NW. A Gaussian curve was then fitted to this line section using the curve fitting tool in MATLAB. The number of pixels contained within the full width at half maximum of the Gaussian curve was chosen as the NW width. This width and a user defined distance along the NW were used to create an area of interest for the NW in the difference image. Pixels within this area were then averaged in the direction perpendicular to the NW, thereby creating a width averaged line section which covered a user defined distance along the NW in units of pixels, as shown in Fig. 5D. The physical distance in micrometer was obtained from the known dimensions of a pixel for a typical scan area of 10 x 10 μm and pixel resolution of 256 x 256 pixels.

Data Analysis Routine

The SPP propagation distance was determined by fitting the width averaged line sections to the following model, which considered the MEH-PPV photobleaching as a first order decay reaction due to two components: direct laser excitation at one end of the gold NW modeled by a Gaussian intensity profile and indirect excitation through plasmon-exciton coupling between the MEH-PPV and the exponentially decaying SPP near-field along the gold NW. The MEH-PPV concentration as a function of time t is given by:

$$\frac{[MEH-PPV]_t}{[MEH-PPV]_0} = \exp(-kI_G(x)t - kI_{SPP}(x)t) \qquad \textbf{Eq. 1}$$

Here $[MEH\text{-}PPV]_0$ and $[MEH\text{-}PPV]_t$ are the initial concentration of MEH-PPV and the concentration at time, t. kI_{SPP}, and kI_G are the products of the photobleaching rate constant k of MEH-PPV and the incident intensities due to the SPP near-field and the Gaussian laser excitation, respectively. The intensities for both processes are given by spatially varying functions assuming an exponential decay of the SPP intensity along the NW and a Gaussian profile for the laser beam according to:

$$I_{SPP}(x) = I_{SPP,0}\exp(-x/x_0) \qquad \textbf{Eq. 2}$$

$$I_G(x) = I_{G,0}\exp(-x^2/\sigma^2) \qquad \textbf{Eq. 3}$$

x_0 is the inverse propagation distance of the SPP and σ the width of the Gaussian laser beam. By inserting Eqs. 2 and 3 into Eq. 1, the following expression for the time varying concentration of fluorescent MEH-PPV species is obtained:

$$\frac{[MEH-PPV]_t}{[MEH-PPV]_0} = \exp\left(-kI_{G,0}t\exp(-x^2/\sigma^2) - kI_{SPP,0}t\exp(-x/x_0)\right) \qquad \textbf{Eq. 4}$$

The bleach intensity as a function of x and t as measured in the BlIPP experiments is then given by:

$$I_{bleaching}(x,t) = 1 - \exp\left(-kI_{G,0}t\exp\left(-x^2/\sigma^2\right) - kI_{SPP,0}t\exp\left(-x/x_0\right)\right) \qquad \textbf{Eq. 5}$$

The fits in Figures 5 and 6 (shown in the next section) were created by fitting Eq. 5 and adjusting the variables x_0, $kI_{SPP,0}$, and $kI_{G,0}$ to obtain the best agreement with the experimental data. This model well describes the experimental photobleach intensity profiles and accounts for the contributions from both the direct laser excitation and the SPP near-field. In particular, the increasing offset for BlIPP experiments as a function of exposure time, t for the same gold NW is well explained by this model yielding the same propagation distance for each image. We also verified that $kI_{SPP,0}$ does not depend on the radial distance from the NW in the x,y sample plane by comparing the results between width averaged line sections with photobleach intensity profiles that were taken along the center of the NW and not averaged over the NW width.

Results from BIIPP Experiments

Fig. 6A shows a confocal fluorescence image of a gold NW that has been coated with a 60 nm thick film of MEH-PPV. Excitation was carried out with a circularly polarized 532 nm laser coupled into an inverted single-molecule microscope equipped with a scanning stage and an avalanche photodiode. The gold NWs used in this study had an average length and thickness of 6.1 μm and 400 nm, respectively. At a wavelength of 532 nm these NWs were too long to cause observable distal end emission due to SPP propagation. The gold NW in Fig. 6A is visible because the fluorescence of the MEH-PPV is enhanced by the plasmonic near-field compared to the background.[24-27] Fluorescence enhancement near plasmonic nanoparticles depends strongly on the distance to the metal surface as at very close separations the fluorescence is instead quenched.[24, 28] Although the distance between the MEH-PPV film and the gold NW was not controlled, direct contact between MEH-PPV and the gold was avoided by the presence of the CTAB coating of the chemically prepared NWs. We calculated a fluorescence enhancement factor of 3 by taking the ratio of the background signal and the intensity at the center of the NW.

To investigate SPP propagation for the gold NW in Fig. 6, we first positioned the sample such that the laser was focused at the left NW end. After raising the laser power to 40 nW, the NW was exposed to continuous excitation with 532 nm light for 9 min, which was followed by acquiring a second fluorescence image at the initial power of 4 pW. As shown in Fig. 6B, the fluorescence intensity of the MEH-PPV film decreased to about zero in a circular area around the left NW end, which can be assigned to photobleaching of the MEH-PPV due to direct photoexcitation by the 532 nm laser.

However, a closer inspection of the fluorescence image in Fig. 6B furthermore reveals that the MEH-PPV film was also photobleached along the NW, but in no other directions from the laser spot. To better visualize this effect, image Fig. 6B was subtracted from panel A, creating a difference image given in Fig. 6C, where a higher intensity corresponds to a larger degree of MEH-PPV photobleaching.

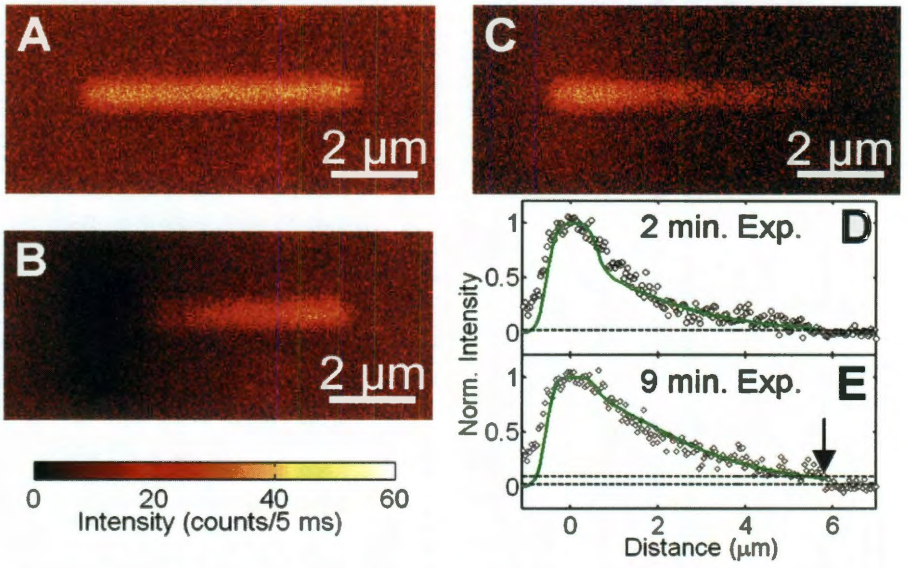

Fig. 6 Confocal fluorescence images recorded with 4 pWof 532 nm laser light for a MEH-PPV coated 6 µm long gold NW before **(A)** and after **(B)** continuous excitation of the left NW end for 9 min with a power of 40 nW. **(C)** Difference image generated by subtracting (B) from (A). **(D)** Width averaged intensity line section (points) taken along the long NW axis from a difference image taken after a 2 min exposure. The green line is a fit to the data yielding a SPP propagation distance of 1.7 µm.. **(E)** Width averaged line section (points) and fit (green line) obtained from the difference image shown in (C) for a 9 min exposure time. The arrow marks the end of the NW where after the longer exposure time an offset in the photobleached intensity became visible due to continued SPP aided photobleaching. The recovered SPP propagation distance remained unchanged consistent with the described photobleaching mechanism.

The SPP near-field can be related to the photobleach intensity in Fig. 6C. While the laser was focused on the NW end, SPPs were excited and propagated along the NW. The SPPs interacted with the MEH-PPV through plasmon-exciton coupling.[29-31] The excitations in the MEH-PPV film then decay radiatively by fluorescence or through nonradiative channels, which include a small but significant yield of irreversible photochemical reactions permanently turning off the MEH-PPV fluorescence

(photobleaching). The concentration of photobleached polymers as measured by the photobleach intensity is directly related to the rate of photobleaching and the spatial distribution of the incident excitation intensity, which is governed by the laser power, strength of the plasmonic near-field, and the exposure time.

The effect of the exposure time is illustrated in Fig. 6D,E, which shows the width averaged line sections along the major NW axis taken from the difference images after exposure times of 2 (Fig. 6D) and 9 (Fig. 6E) min. The photobleach intensity profiles consisted of contributions from the direct laser excitation at the left NW end and the indirect excitation of the MEH-PPV film through plasmon-exciton interactions. Direct photobleaching by the laser was more efficient as can be seen from the complete bleaching of the MEH-PPV within the laser spot even for the shortest exposure time. In contrast, because of the much weaker indirect excitation of the MEH-PPV by the plasmonic near-field, the degree of bleaching increased with time. As indicated by the arrow in Fig. 6E, this can be seen by the offset in the photobleach intensity at the right NW end. A higher laser power had the same effect as a longer exposure time as the laser power determined the initial amplitude of the SPP modes (data not shown).

Assuming that the rate of MEH-PPV photobleaching as a function of incident intensity follows a first order decay process, the measured photobleach intensity along the NWs can be quantitatively described by considering the contributions from direct laser excitation and the SPP near-field. The laser intensity was modeled by a Gaussian profile and the damping of the SPPs along the NWs by an exponential function.[10] The fit using Eq. 5 then yielded the same SPP propagation distance of 1.7 μm for the 2 and 9 min exposure times. The independence of the SSP propagation distance on the exposure time

and the drop in photobleach intensity at the right NW end are furthermore consistent with the described plasmon-exciton mediated photobleaching mechanism.

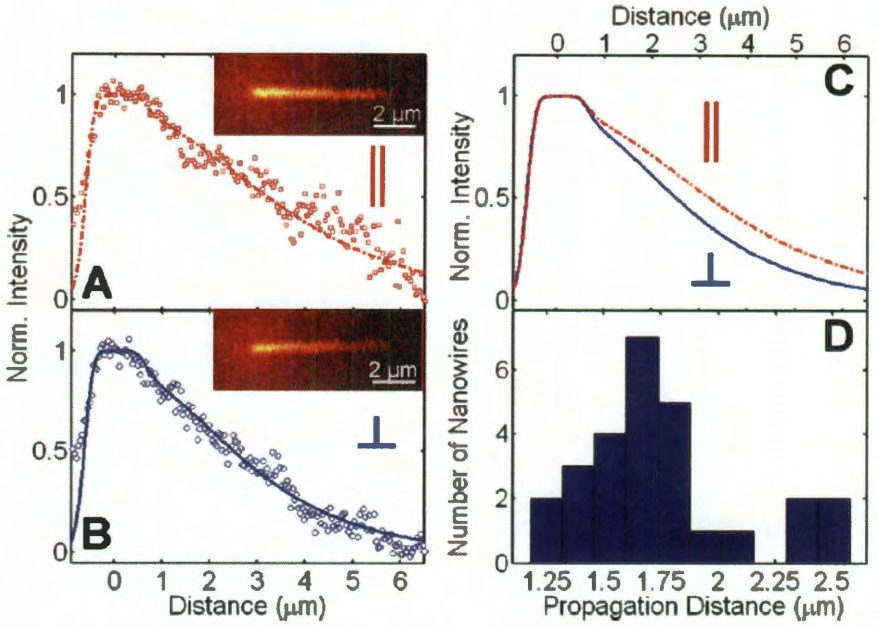

Fig. 7 Width-averaged intensity line sections and fits obtained from the difference images shown in the insets for excitation polarization parallel **(A)** and perpendicular **(B)** to the long NW axis. The difference images were obtained after 8 min exposure to an excitation power of 90 nW. For the fluorescence imaging a laser power of 9 pW was used. **(C)** Comparison of the fits to the plasmon bleach intensity for the two NWs shown in (A) and (B). The larger offset for parallel polarized excitation (red) indicates a larger SPP amplitude for this polarization. **(D)** Histogram of SPP propagation distances measured by BIIPP for 27 individual gold NWs.

To characterize the nature of the SPP modes in these gold NWs, we performed BIIPP experiments with excitation polarized parallel and perpendicular to the main NW axis as shown in Fig. 7A,B, respectively. The insets show the difference images for two NWs with similar lengths and the same exposure time of 8 min and laser power of 90 nW. The fluorescence enhancement was found to be independent of laser polarization (Fig. 4) and no further corrections were necessary. The fits to the experimental data in Fig. 7A,B give SPP propagation distances of 2.1 and 1.7 μm, respectively. The mean SPP propagation distances as obtained from a total of 20 NWs were 1.9 ± 0.4 and 1.7 ± 0.2 μm for parallel and perpendicular excitation, suggesting that the SPP propagation

distance is only weakly dependent on the excitation polarization. However, a direct comparison of the fits shown in Figure 6C reveals that the amplitude of the SPP near-field is larger for excitation with parallel polarized light because of the larger offset in the photobleach intensity. These measurements demonstrate that although both longitudinal and transverse polarized SPPs were excited, parallel excitation was more efficient.

The histogram in Fig. 7D summarizes the SPP propagation distances obtained for 27 independent BlIPP measurements on gold NWs. The average propagation distance was 1.8 ± 0.4 μm. The width of the distribution can be attributed to several factors including the variation in NW diameters and tip shape as well as differences in surface roughness which influence the confinement and damping of the SPP modes.[4, 10] In addition, the MEH-PPV film thickness and homogeneity including locally varying polymer chain conformations could cause changes in the MEH-PPV photobleaching rate and hence affect the fitted SPP propagation distances.

Finite difference time domain (FDTD) simulations

To further verify our experimental results we performed finite difference time domain (FDTD) simulations, the results of which are shown in Figure 7. A Gaussian excitation beam with parallel (Fig. 8A) and perpendicular (Fig. 8B) polarization coupled to several SPP modes at the left NW tip. The initial decay of the electric field intensity was due to a superposition of mostly localized and higher order multipolar surface plasmons. At 1 μm from the NW tip, the dominant SPP with a propagation distance of 1.1 μm was the m = 2 mode as identified by cross sectional views of the surface charge distribution. In agreement with experiment, this quadrupole SPP mode could be excited with parallel and perpendicular polarization, slightly favoring parallel excitation as seen by the larger amplitude. A weaker m = 1 SPP mode with an even longer propagation distance of 4 μm was also supported by this NW. The length of the simulated NW was chosen to be 10 μm in Fig. 8 to clearly identify the m = 1 mode.

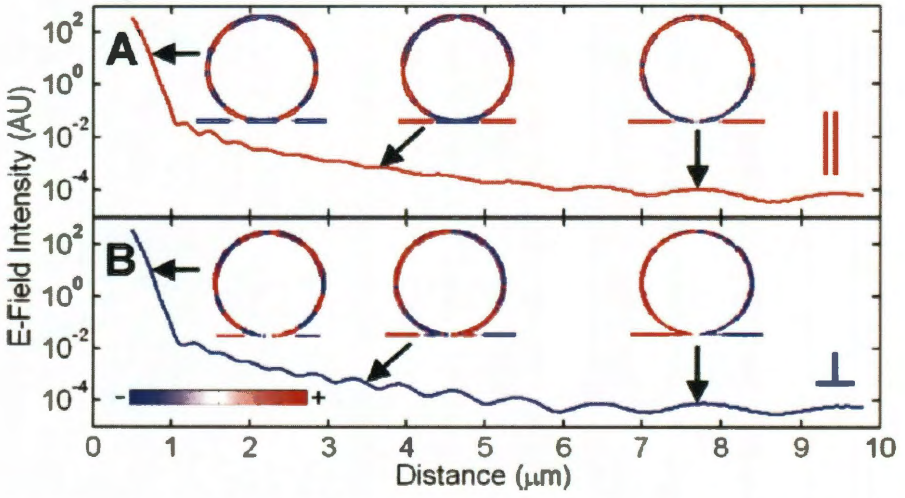

Fig. 8 FDTD simulations for a 400 nm thick gold NW with a 532 nm Gaussian laser beam (fwhm = 330 nm) having parallel (**A**) and perpendicular (**B**) polarization incident on the left NW end. Several SPP modes were excited and identified based on their surface charge distributions. Cross sectional views of the surface charges are shown as insets, where the scale from red to blue represents changes from positive to negative. The fast decay of the electric field intensity at the NW tip can be assigned to a mixture of mostly localized plasmon modes. Further along the NW the dominant SPP is the m = 2 mode followed by a less intense and slower decaying m = 1 SPP.

While the m = 2 SPP is the dominant mode, the m = 1 mode also contributed to the measured averaged propagation distance of 1.8 μm. In particular, the relative amplitudes of these two modes depend critically on the NW diameter as well as the shape of the NW tip.[4] The latter strongly determines the coupling efficiency of the laser light to different SPP modes. FDTD simulations for different gold NW diameters, the smallest of which 120 nm diameter is shown in Fig. 9, furthermore show that the m = 1 SPP mode starts to dominate for thinner NWs as the m = 2 mode could no longer be supported. Interestingly, the fundamental m = 0 mode was always strongly localized at the NW tip with a large damping yielding sub-micrometer propagation distances independent of NW diameter.

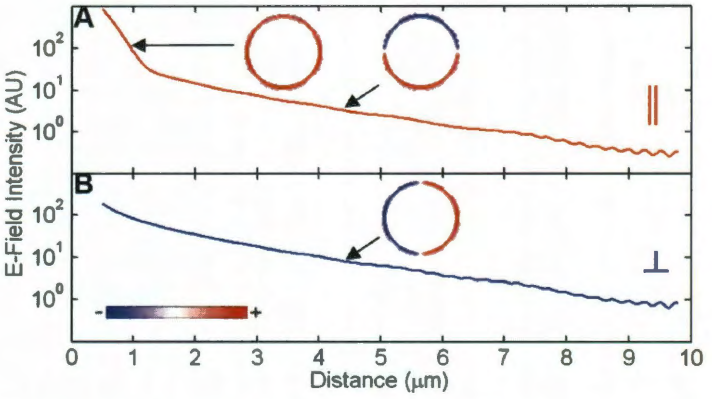

Fig. 9 FDTD simulations for a 120 nm thick gold NW with a 532 nm plane wave having parallel **(A)** and perpendicular **(B)** polarization incident on the left NW end. The length of the NW was 10 μm. Cross sectional views of the surface charges for the NW in a vacuum medium are shown as insets, where the scale from red to blue represents changes from positive to negative. The main decay of the electric field intensity for parallel and perpendicular excitation can be assigned to the m =1 SPP with a propagation distance of 2.0 mm for both polarizations. The fast decay for parallel polarization corresponds to the m = 0 SPP mode, which is localized at the NW tip. Fitting a decay constant for the m = 0 mode is difficult because of the overlap with localized plasmons excited by the plane wave.

Because the FDTD simulations treated the MEH-PPV film as a simple dielectric, the interactions between NW plasmons and MEH-PPV excitons were entirely neglected. Hence, possible gain due to conversion of excitons back into plasmons along the NW effectively increasing the SPP propagation distance were not taken into account and

could also explain the longer SPP propagation distance in the BlIPP studies. However, the good agreement between the FDTD calculations and the experimental and modeled photobleach intensity line sections for all NWs including time dependent BlIPP measurements on the same NWs suggests that gain, if at all, was only a minor contributor to the measured SPP propagation distance. A laser power dependence on the fluorescence spectra also showed no spectral narrowing indicative of stimulated emission and gain.[32]

Conclusion

In summary, we report a new method, BlIPP, by which it is possible to visualize SPP propagation in the far-field via plasmon-exciton coupling mediated photobleaching of an organic chromophore coated on top of a plasmonic waveguide. BlIPP creates a permanent record of the spatial intensity profile of the SPP near-field, particularly suited to read out short SPP propagation distances without the interference by a much stronger signal from the excitation source. We applied BlIPP to visualize SPPs in chemically prepared highly crystalline 6.1 μm × 400 nm gold NWs. Even for a wavelength of 532 nm, where interband absorption losses are significant in gold, we found a propagation distance of 1.8 ± 0.4 μm. These results are in very good agreement with FDTD simulations and the analysis of the surface charge distribution revealed that the main SPP is a quadrupole mode that can only be supported by these thicker NWs. We expect that the simplicity of the BlIPP method, and its utility in investigating even strongly damped SPPs, will make it a useful tool to determine SPP propagation distances in a wide range of plasmonic materials.

References:

1. Ditlbacher, H.; Hohenau, A.; Wagner, D.; Kreibig, U.; Rogers, M.; Hofer, F.; Aussenegg, F. R.; Krenn, J. R. *Physical Review Letters* **2005,** 95, (25), 257403.
2. Dickson, R. M.; Lyon, L. A. *Journal of Physical Chemistry B* **2000,** 104, (26), 6095-6098.
3. Yan, R. X.; Pausauskie, P.; Huang, J. X.; Yang, P. D. *Proceedings of the National Academy of Sciences of the United States of America* **2009,** 106, (50), 21045-21050.
4. Li, Z. P.; Bao, K.; Fang, Y. R.; Huang, Y. Z.; Nordlander, P.; Xu, H. X. *Nano Letters* **2010,** 10, (5), 1831-1835.
5. Sanders, A. W.; Routenberg, D. A.; Wiley, B. J.; Xia, Y. N.; Dufresne, E. R.; Reed, M. A. *Nano Letters* **2006,** 6, (8), 1822-1826.
6. Staleva, H.; Skrabalak, S. E.; Carey, C. R.; Kosel, T.; Xia, Y. N.; Hartland, G. V. *Physical Chemistry Chemical Physics* **2009,** 11, (28), 5889-5896.
7. Lamprecht, B.; Krenn, J. R.; Schider, G.; Ditlbacher, H.; Salerno, M.; Felidj, N.; Leitner, A.; Aussenegg, F. R.; Weeber, J. C. *Applied Physics Letters* **2001,** 79, (1), 51-53.
8. Maier, S. A.; Kik, P. G.; Atwater, H. A.; Meltzer, S.; Harel, E.; Koel, B. E.; Requicha, A. A. G. *Nature Materials* **2003,** 2, (4), 229-232.
9. Maier, S. A.; Brongersma, M. L.; Kik, P. G.; Meltzer, S.; Requicha, A. A. G.; Atwater, H. A. *Advanced Materials* **2001,** 13, (19), 1501-1505.
10. Raether, H. *Springer Tracts in Modern Physics* **1988,** 111, 1-133.
11. Barnes, W. L. *Journal of Optics A: Pure and Applied Optics* **2006,** 8, (4), S87-S93.
12. Krenn, J. R.; Weeber, J. C. *Philosophical Transactions of the Royal Society of London Series a-Mathematical Physical and Engineering Sciences* **2004,** 362, (1817), 739-756.
13. Johnson, P. B.; Christy, R. W. *Physical Review B* **1972,** 6, (12), 4370.
14. Wiley, B. J.; Lipomi, D. J.; Bao, J. M.; Capasso, F.; Whitesides, G. M. *Nano Letters* **2008,** 8, (9), 3023-3028.
15. Allione, M.; Temnov, V. V.; Fedutik, Y.; Woggon, U.; Artemyev, M. V. *Nano Letters* **2008,** 8, (1), 31-35.
16. Dorfmuller, J.; Vogelgesang, R.; Weitz, R. T.; Rockstuhl, C.; Etrich, C.; Pertsch, T.; Lederer, F.; Kern, K. *Nano Letters* **2009,** 9, (6), 2372-2377.
17. Knight, M. W.; Grady, N. K.; Bardhan, R.; Hao, F.; Nordlander, P.; Halas, N. J. *Nano Letters* **2007,** 7, (8), 2346-2350.
18. Verhagen, E.; Spasenovic, M.; Polman, A.; Kuipers, L. *Physical Review Letters* **2009,** 102, (20), 4.
19. Douillard, L.; Charra, F.; Korczak, Z.; Bachelot, R.; Kostcheev, S.; Lerondel, G.; Adam, P. M.; Royer, P. *Nano Letters* **2008,** 8, (3), 935-940.
20. Ditlbacher, H.; Krenn, J. R.; Felidj, N.; Lamprecht, B.; Schider, G.; Salerno, M.; Leitner, A.; Aussenegg, F. R. *Applied Physics Letters* **2002,** 80, (3), 404-406.
21. Graff, A.; Wagner, D.; Ditlbacher, H.; Kreibig, U. *European Physical Journal D* **2005,** 34, (1-3), 263-269.
22. Solis, D.; Chang, W. S.; Khanal, B. P.; Bao, K.; Nordlander, P.; Zubarev, E. R.; Link, S. *Nano Letters* **2010,** 10, (9), 3482-3485.

23. Khanal, B. P.; Zubarev, E. R. *Journal of the American Chemical Society* **2008,** 130, (38), 12634-12635.
24. Anger, P.; Bharadwaj, P.; Novotny, L. *Physical Review Letters* **2006,** 96, (11), 113002.
25. Chen, Y.; Munechika, K.; Ginger, D. S. *Nano Letters* **2007,** 7, (3), 690-696.
26. Chan, Y. H.; Chen, J. X.; Wark, S. E.; Skiles, S. L.; Son, D. H.; Batteas, J. D. *ACS Nano* **2009,** 3, (7), 1735-1744.
27. Kinkhabwala, A.; Yu, Z. F.; Fan, S. H.; Avlasevich, Y.; Mullen, K.; Moerner, W. E. *Nature Photonics* **2009,** 3, (11), 654-657.
28. Seelig, J.; Leslie, K.; Renn, A.; Kuhn, S.; Jacobsen, V.; van de Corput, M.; Wyman, C.; Sandoghdar, V. *Nano Letters* **2007,** 7, (3), 685-689.
29. Akimov, A. V.; Mukherjee, A.; Yu, C. L.; Chang, D. E.; Zibrov, A. S.; Hemmer, P. R.; Park, H.; Lukin, M. D. *Nature* **2007,** 450, (7168), 402-406.
30. Fedutik, Y.; Temnov, V. V.; Schops, O.; Woggon, U.; Artemyev, M. V. *Physical Review Letters* **2007,** 99, (13), 4.
31. Wei, H.; Ratchford, D.; Li, X. Q.; Xu, H. X.; Shih, C. K. *Nano Letters* **2009,** 9, (12), 4168-4171.
32. Noginov, M. A.; Zhu, G.; Belgrave, A. M.; Bakker, R.; Shalaev, V. M.; Narimanov, E. E.; Stout, S.; Herz, E.; Suteewong, T.; Wiesner, U. *Nature* **2009,** 460, (7259), 1110-1112.